Ion radiation albedo effect: influence of surface roughness on ion implantation and sputtering of materials

Ion radiation albedo effect: influence of surface roughness on ion implantation and sputtering of materials

Yonggang Li[1,2,4], Yang Yang[2], Michael P. Short[2*], Zejun Ding[3], Zhi Zeng[1,4*] and Ju Li[2,5*]

[1] Key Laboratory for Materials Physics, Institute of Solid State Physics, Chinese Academy of Sciences, Hefei, 230031, China.

[2] Department of Nuclear Science and Engineering, Massachusetts Institute of Technology, Cambridge, Massachusetts, 02139, USA.

[3] Hefei National Laboratory for Physical Sciences at Microscale and Department of Physics, University of Science and Technology of China, Hefei, 230026, P. R. China.

[4] University of Science and Technology of China, Hefei, 230026, P. R. China.

[5] Department of Materials Science and Engineering, Massachusetts Institute of Technology, Cambridge, Massachusetts, 02139, USA.

[*]E-mail: zzeng@theory.issp.ac.cn; hereiam@mit.edu; liju@mit.edu.

Abstract. In fusion devices, ion retention and sputtering of materials are major concerns for the selection of compatible plasma-facing materials (PFMs) especially in the context of their microstructural conditions and surface morphologies. We demonstrate how surface roughness changes ion implantation and sputtering of materials under energetic ion irradiation. Using a new, sophisticated 3D Monte Carlo code (IM3D) and a random rough surface model, the ion implantation and sputtering yields of tungsten with surface roughness varying between 0-2 μm have been studied for irradiation by 0.1-1 keV D^+, He^+ and Ar^+ ions. It is found that both ion backscattering and sputtering yields decrease with increasing roughness, hereafter called the ion radiation albedo effect. This effect is mainly dominated by the direct, line-of-sight deposition of a fraction of emitted atoms onto neighboring asperities. Backscattering and sputtering increase with more oblique irradiation angles. We propose a simple analytical formula to relate rough-surface and smooth-surface results.

Keywords: Ion radiation albedo effect, surface roughness, ion implantation and sputtering, Plasma-facing materials, Monte Carlo

1. Introduction

Ion beam and plasma processing are widely used to tailor the geometric, mechanical, electronic, magnetic, and optical properties of materials [1, 2]. Ion irradiation induces serious radiation damage [3, 4], while plasma-surface interactions (PSIs) affect the lifetime of the plasma-facing materials (PFMs) in fusion reactors by inducing changes in surface roughness and thermal transport, potentially evaporating PFMs to degrade or quench the core plasma. Ion (D/T/He) retention and sputtering of PFMs are therefore major concerns for the selection of compatible PFMs in fusion reactors [5-8]. PFMs in proposed fusion reactors must withstand low-energy (10-1000 eV), high flux (up to 10^{24} $m^{-2}s^{-1}$) D/T/He ions, high-energy neutrons (14.1 MeV) as well as high heat fluxes up to 20 MWm^{-2} [7]. The surface morphology of PFMs is dramatically modified, forming features like mounds, fuzz, bubbles, pores, and blisters [8]. These surface features, with a characteristic length scale L_R comparable to the ion penetration depth L_I, can significantly affect the ion retention and sputtering of PFMs. This in turn would affect the further evolution of PFM surfaces, creating a complex, positive-feedback evolution of PFM surface roughness.

In general, tungsten (W) surface features under high fluxes of low energy He-ion irradiation are attributed to bubble bursting and/or loop punching caused by He-induced void growth and physical sputtering [9, 10]. High implantation of He atoms is also one of the key factors for bubble growth, as inert gases stabilize radiation void nuclei, and the subsequent formation of “tungsten fuzz” [11]. He-induced W surface nanostructures have thus been recognized as a potential drawback for W as a PFM, due to their inducing fragility, degraded thermal transport, and the potential enhancement of ion/fuel retention [12]. In a different context, techniques which employ surface structuring by energetic ion bombardment, including ion beam sputtering [13] and low energy He-ion irradiation [2], are established surface processing techniques. For example, due to their high porosity (up to 90%), surface fuzzy structures manifest their potential in various applications requiring high surface area and light absorption [2, 14]. However, the resulting complex surface morphology and its effects on surface sputtering and erosion, H isotope trapping and release, have not been fully addressed [15]. Experimental studies show that it is rather difficult to rely on a single quantity to predict the behavior of materials after ion/plasma exposure [2]. It is therefore essential to understand the fundamental and practical aspects of irradiated materials in the context of their microstructural conditions and surface morphologies [15].

Recent studies have found that ion retention [16] and physical sputtering [2, 12, 17-21] respectively increase and decrease due to surface roughening. While the behaviors of ion retention and sputtering of smooth materials under different conditions have been well-studied, including ion energy [6], flux [22], fluence [22, 23], incident angle [24], sample temperature [22-24] and existing defects [24], much less is known regarding the effects of surface roughness and porosity on ion retention/implantation and sputtering of materials [16, 25]. Because L_I is typically 1-10 nm, surface nanoporosity or nanofeatures should change a surface's ion "albedo."

Recently, the enhancement of ion retention by surface roughness has been indicated by deuterium (D) retention experiments in pre-damaged W [16]. Trapping of significant amounts of D should take place in or close to the blister/protrusion in W pre-damaged by implantation with MeV ions, and give rise to an additional peak in the thermal desorption spectrum at 700 K [16]. This increased D retention is mainly caused by the creation of defect sites/sinks like dislocations around the blister cavities. In general rough surfaces features reduce D retention due to shorter diffusion pathways to the surface and thus higher D effusion from these surfaces. The influence of roughness on out-diffusion is larger than that on implantation. But if the contribution of D diffusion and trapping to desorption is fixed, the ion implantation increase would be the only key factor left to affect D retention. Reduced sputtering from rough/fuzzy surfaces has also been recently reported. Based on mass loss measurements, Nishijima et al. have shown that the sputtering yield of fuzzy W surfaces under 110 eV Ar-ion sputtering decreases with increasing fuzz thickness and saturates at about 10% of that of a smooth surface [12]. They attributed the reduction in sputtering yield to the direct line-of-sight deposition of sputtered W atoms onto neighboring fuzz before ejection into the plasma. Tanyeli *et al*. also showed that their measured values of the sputtering yield of metals with He-induced surface modifications are around one order of magnitude below the expected one, due to the effect of surface morphology [2]. Doerner et al. [18-21] have systematically investigated the influence of surface morphology on sputtering of beryllium (Be), for pure Be exposed to high-flux [18] and high fluence [19] un-seeded [19] or Be-impurity seeded D plasma [18, 20, 21] at room or elevated temperatures [21]. They also found that Be erosion by D plasma results in the development of cone/grass-like surface morphology. The resultant measured erosion rate is almost an order of magnitude less than expected from simple sputtering calculations, mainly due to deposition of some sputtered atoms on adjacent cones.

In fact, at energies sufficiently above the sputtering threshold energy, Sigmund's theory already proposes curvature-dependent sputtering [26]. Based on Sigmund's theory, and assuming symmetric surface structures, an analytical formula for morphology-dependent sputtering yield predicts a decrease in sputtering yield with curvature [17]. However, real morphological changes are more complex compared to a symmetrical structure defined by a finite number of parameters, thus a larger deviation between calculated and experimental data is expected [2].

Therefore, modeling the relations between ion implantation increase/sputtering decrease and surface roughness evolution is necessary, though computationally challenging. Monte Carlo (MC) simulations can predict some ion implantation and sputtering behavior, showing the effects of roughness on sputtering yield [27-31]. In particular, the fractal rough surface models have been introduced into MC simulations [29-31] to capture more features of rough surfaces. Ruzic added the fractal geometry composed of an exact self-similar fractal into VF-TRIM code [29]. Kenmotsu et al. also incorporated the two-dimensional fractal surface model into their ACAT code [30], and set the fractal dimension to 2.1 to fit the experimental data. Recently, Hu et al. developed a new fractal version of ITMC-F to study the impact of surface roughness on the angular dependence of sputtering yields, based on random fractal surfaces generated by midpoint displacement algorithm in computer graphics and support vector machine algorithm in pattern recognition [31]. However, these fractal rough surface models are either over-simplified with the overall effect other than the local effect of fractal rough surfaces [29] or relatively more complicated with several adjustable fitting parameters [30, 31]. Established common codes like SRIM [32] still cannot treat strongly anisotropic structures, such as nanostructures and roughness. In addition, nearly all of these models emphasize the influence of incident angles on sputtering. Thus, the dependence of ion implantation and sputtering yields on surface roughness should be studied more realistically and systematically.

By using the more advanced IM3D code [33], a general and robust approach has been developed to analyze ion radiation damage and corresponding 3D spatial distributions of primary defects in nanostructured materials under ion beam irradiation. In this work, we propose a general rough surface geometry model based on the Finite Element Triangular Mesh (FETM) algorithm [34] and successfully couple it into IM3D, creating a way to reveal the effects of surface roughness on ion implantation and sputtering in detail. Note that IM3D can track the processes (like ion implantation and sputtering) at the timescales of less than about 10 picoseconds (*ps*) in general. Another key process at longer timescales, namely the formation of surface roughness in equilibrium with the erosion and deposition by the incident beam, is beyond the scope of this paper and not investigated.

2. Methods

All simulations are performed with IM3D [33] using the “Full Cascades (FC)” option, as shown below. This is always adopted to follow the tracks of all ions and subsequent cascades using the binary collision approximation (BCA), since the “Quick Kinchin-Pease (QKP)” [35, 36] option does not produce information regarding the angular distribution of sputtered atoms. In addition, when the material feature size scale becomes nano-scale, the nano-energetic and nano-geometric effects can take place in collision cascades, as discussed in the supplementary material (SOM 1). For objects smaller than 20 nm, both of these two effects must be taken into account, while for objects >20 nm, the nano-energetic effect is less important. Since in most cases the feature size of roughness/fuzz induced by irradiation is in the range of 10’s nm [37], the nano-energetic effect may be neglected.

2.1 IM3D code

An open-source parallel 3D MC code, IM3D, is developed for simulating the transport of ions through and the production of defects within nanostructured materials with excellent parallel scaling performance [33]. IM3D is based on fast indexing of scattering integrals and SRIM stopping power database, and allows the user a choice of Constructive Solid Geometry (CSG) [38, 39] or Finite Element Triangular Mesh (FETM) [34, 40] method for constructing 3D shapes and microstructures. It can thus model arbitrarily complex 3D targets made of different geometric elements, each composing of different materials. In addition, the generation of point defects (i.e., interstitials and vacancies) can be modeled alternatively by the "Quick Kinchin-Pease (QKP)" [35, 36] and "Full Cascades (FC)" options. Both the 3D spatial distribution of ions and also the kinetic phenomena associated with the ion's energy loss, such as amorphization, damage, sputtering, ionization, and phonon production, can be calculated rapidly by IM3D while following all target atom cascades in detail. Different output parameters can thus be given, including electronic and nuclear energy deposition, back-scattering/implanted ions, radiation dose in DPA (displacements per atom), point defect concentrations, and sputtered atoms, etc. For 2D films and multilayers, IM3D perfectly reproduces SRIM calculation results, and can be ~10^2 times faster in serial execution and >10^4 times faster using Beowulf parallel computer. For 3D problems, it provides a fast approach for analyzing the spatial distributions of primary displacements and defect generation under ion irradiation. In general, a typical simulation of 10^5 ions in total with energies of keV to MeV consumes only seconds to minutes on a Beowulf cluster even for complex 3D geometry.

2.2 Rough surface generation

A simple rough surface geometry model based on the FETM approach is chosen here, reproducing the typical features of a rough surface as shown in SOM 2. Specifically, the height of each mesh point, *Z*, on a square mesh with lattice constant *a* (figure 1(a)), is sampled following the truncated Gaussian distribution:

$$f(Z) \propto \exp\left(-Z^2/2\sigma^2\right),\ Z \in \left[-3\sigma, 3\sigma\right]. \tag{1}$$

Each square is then divided into two triangular elements by randomly selecting the diagonal directions to generate a triangular mesh as shown in figure 1(a). Each peak/valley in a complex polyhedron form is built according to the random height of each mesh point (figure 1(b)), and an isotropic rough surface mesh is thus constructed as shown in figure 1(c). An ensemble of rough surfaces can be constructed by adjusting 3σ and a. When $3\sigma = 0$ nm, the limiting case of a smooth surface is generated.

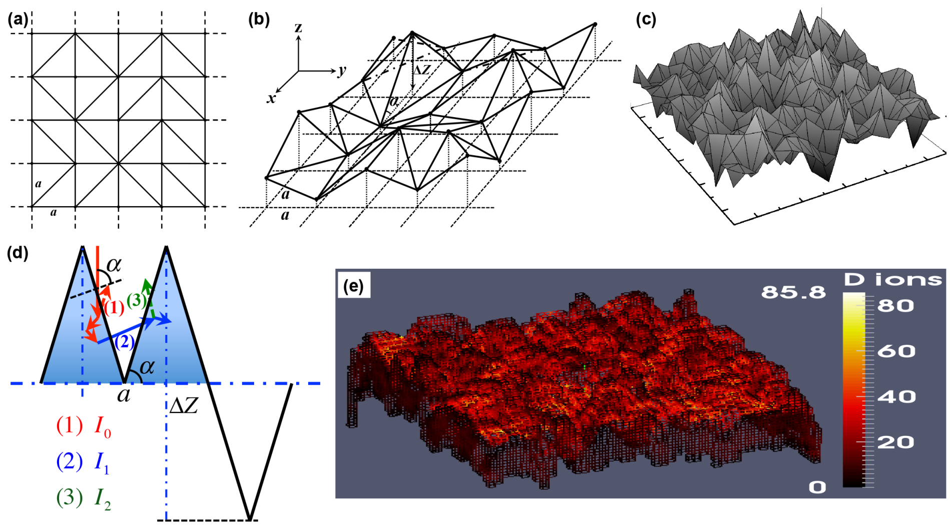

Figure 1. (a) Schematic of the triangular mesh and (b) the polyhedra forming rough peaks, (c) a rough surface constructed by the FETM method, and (d) a typical cross-section of the asperities. (1) I_0, (2) I_1, and (3) I_2 indicate the first backscatters of incident ions from a rough peak, the shading of backscattered ions by an adjacent rough peak, and the secondary backscattering of shaded ions from the adjacent rough peak, respectively. (e) The spatial distribution of D-ion implantation in W rough surface with $3\sigma = 60$ nm and $a = 50$ nm.

Compared to the fractal rough surface model [29-31], this FETM-based geometry model [34] is simpler and more intuitive, and can even reproduce realistic rough surfaces according to the experimental AFM images with only two adjustable parameters (3σ and a) [41]. Furthermore, it is also a feasible and efficient framework for performing IM3D simulations, which can represent real scattering trajectories near rough surfaces and simultaneously take account of the refraction effect of ongoing particles with respected to the local surface normal [33, 34].

3. Results

3.1 Trajectories of ions, recoils and sputtered atoms

The effects of factors like roughness (σ) and angle of incidence (θ) on the primary ion backscattering coefficient (η) and sputtering yield (Y) can therefore be quantitatively simulated. During irradiation, some of the incident ions enter and remain in the matrix, while a fraction η are backscattered from the surface as shown in figure 2(a). In addition, cascade damage in the matrix and sputtering near the surface occur when the incoming ion energy is high enough. These physical processes are shown in figures 2(b) and (c) by tracking the trajectories of ions as well as recoil and sputtering atoms for W bulk with both smooth (3σ = 0 nm) and rough (a = 50 nm, 3σ = 100 nm) surfaces. At glancing incidence ($\theta = 70°$), most of the backscattered ions and sputtered atoms can escape from the smooth surface, while for the rough surface they are re-intercepted by the rough peaks ("shading effect"). Only a small fraction of them may escape, nearly vertically from the rough surface. Thus, the roughness σ and incident angle θ are two key factors to be discussed in detail below. Also, the angular distributions of backscattered ions and sputtered atoms also depend on the roughness, giving the "albedo" and "matte" properties as in optics.

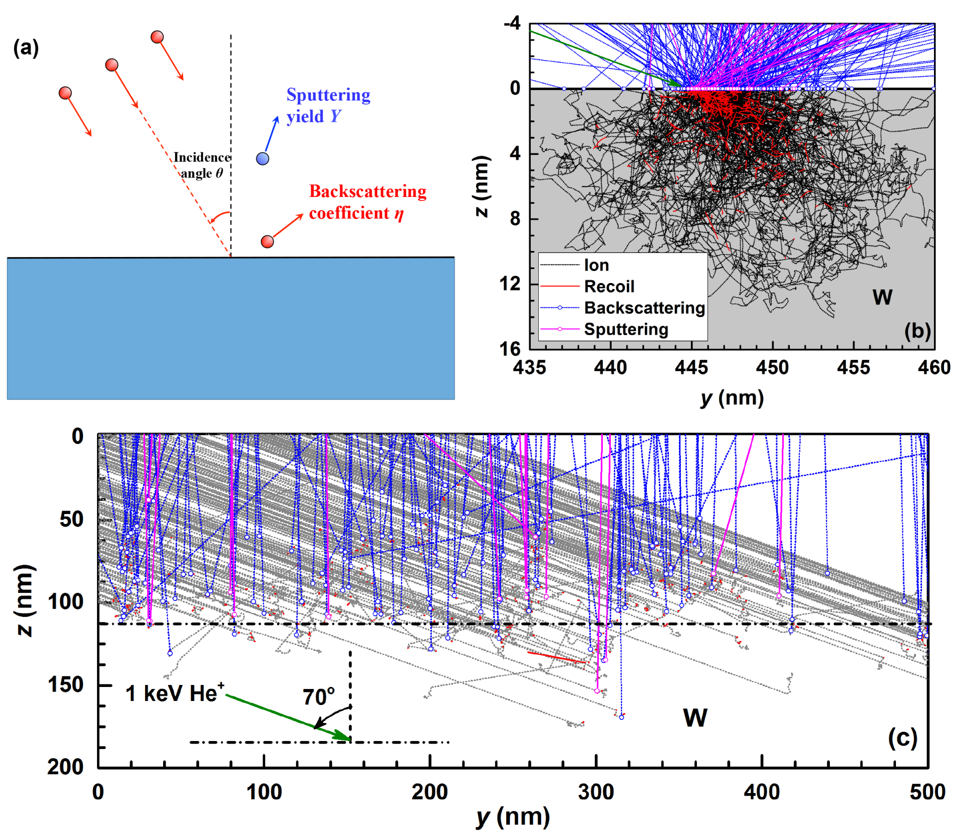

Figure 2. (a) Schematic of ion incidence, backscattering and sputtering processes. The trajectories of ions, recoils, and sputtered atoms for both (b) smooth (3σ=0 nm) and (c) rough (a = 50 nm, 3σ= 100 nm) W surfaces for 300 1 keV He ions at an incident angle of 70° are shown. Single point and random square ion beams are used for the smooth and rough surfaces, respectively. All trajectories are projected onto the *y-z* plane. The scale difference between (b) and (c) is due to the large mismatch between the ion penetration depth L_I (about 12 nm) and the spread characteristic length scale L_R (about 200 nm) of rough surface.

3.2 Smooth W surface

The smooth W surface (3σ = 0 nm) is examined first as a reference. The θ-dependent backscattering coefficient (η) and sputtering yield (Y_0) under 100 eV D- or 1 keV He-ion bombardment are calculated by IM3D, as shown in figure 3. Both η and Y_0 increase with increasing θ except for a small decrease in Y_0 for $\theta > 85°$. The trend is consistent with previous analytical [17], simulation [42-46] and experimental results [45, 47], but with the absolute values a little lower than that of Eckstein's except for Y_0 at glancing incidence. Note that we have taken into account the refraction effect at surfaces/interfaces in IM3D, which should decrease the probability of ion outgoing form surface especially at glancing incidence. Low ion backscattering further causes the increasing of sputtering yields, thus resulting in a higher value of Y_0 at glancing incidence by IM3D compared to that of Eckstein's. The absolute value of η = 0.57 for 100 eV D ions at normal incidence (θ = 0) is a little higher than that of MD [48] due to the excluding of the channeling effect, and reasonably located between values obtained by SRIM-2013 [32] and TRIM.SP [42, 43] due to the differences in the detailed treatment of ion scattering and geometry framework in IM3D. The absolute value of η = 0.47 atoms/ion for 1 keV He ions at θ = 0 is in a reasonable range when comparing with TRIM.SP [42, 43] and experiment [49]. The absolute value of Y_0 = 0.03 atoms/ion for 1 keV He ions at θ = 0 is reasonably located between the values obtained by TRIM.SP [42], MD [46, 50] and experiments [51-58]. Here, default settings are used for simulating of 100 eV D-ion bombardment of W by SRIM-2013 [32]. Note that Eckstein's data compilation [42, 43, 53, 59] is usually considered as the "Gold Standard" for ion reflection and sputtering. SRIM calculations [32] have some known issues like the misestimate of displacement damage [33, 60], the wrong angular distribution of sputtered atom for targets containing low Z elements [45] and the limitations in simulating sputtering yield close to the threshold energy [61]. Anyhow, the absolute values of η and Y_0 will not affect the strength of the nano-geometric effect, as shown below.

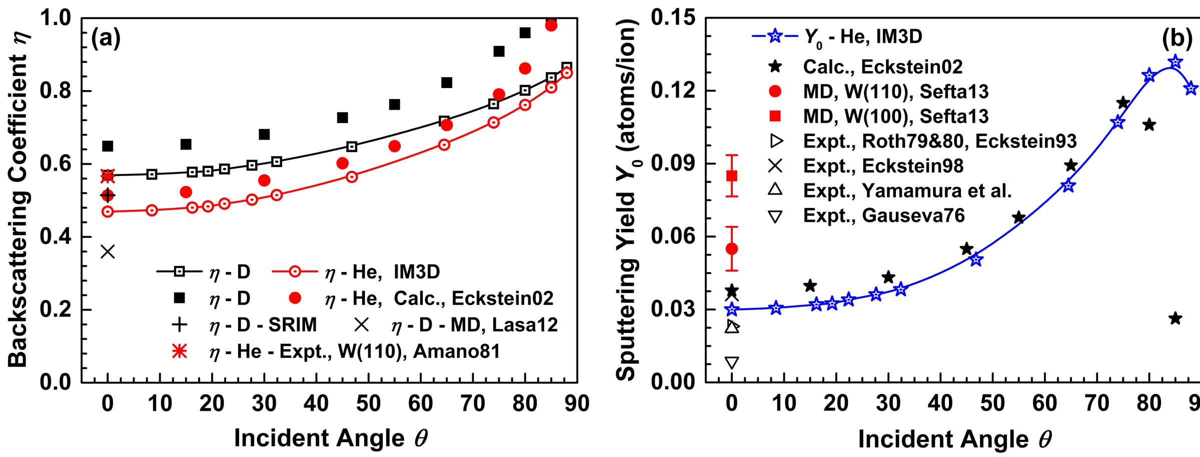

Figure 3. Incident polar angle (θ) dependent (a) backscattering coefficient (η) and (b) sputtering yield (Y_0) of 100 eV D/1 keV He ion bombardment of smooth W surface ($3\sigma = 0$ nm). The SRIM (calculated by SRIM-2013 [32] with default settings), TRIM.SP [42, 43] and MD [48] values of D backscattering coefficient, the TRIM.SP [42, 43] and experimental values [49] of He backscattering coefficient as well as the TRIM.SP [42], MD [46, 50] and experimental values [51-58] of He sputtering yields for smooth surface are also given for comparison. Spline fitting lines are also drawn to guide the reader's eye.

The angular distributions of outgoing ions/atoms' polar (θ') and azimuthal (ϕ') angles for both backscattered and sputtered W atoms are shown in figure 4. The polar angle distribution of outgoing ions/atoms for $\theta = 0$ (red line in figures 4a and 4e)) shows a characteristic sine relationship, $A\sin(2\theta')$, as indicated in previous studies [44, 62]. In addition, the most probable θ' increases with θ, which is also consistent with MD simulations [44]. The ϕ' distribution of backscattered ions is uniform for $\theta = 0$ [44], but it becomes more and more anisotropic with increasing θ. Compared to D-ions, the peaks in the θ', ϕ' distributions of backscattered He-ions are a little sharper. The θ' and ϕ' distributions of sputtered W atoms under 1 keV He-ion irradiation also follow similar trends except for three minor differences: (a) the most probable outgoing θ' is 55° at $\theta > 70°$, (b) a broader peak of ϕ' is near the value of θ, and (c) a small decrease appears at glancing incident angles, as shown in figure 3(b). The sputtering yields, which first increase and then decrease with increasing θ, as well as the anisotropic distribution of sputtering atoms at glancing incidence, are consistent with other predictions [42, 43-45, 53, 59].

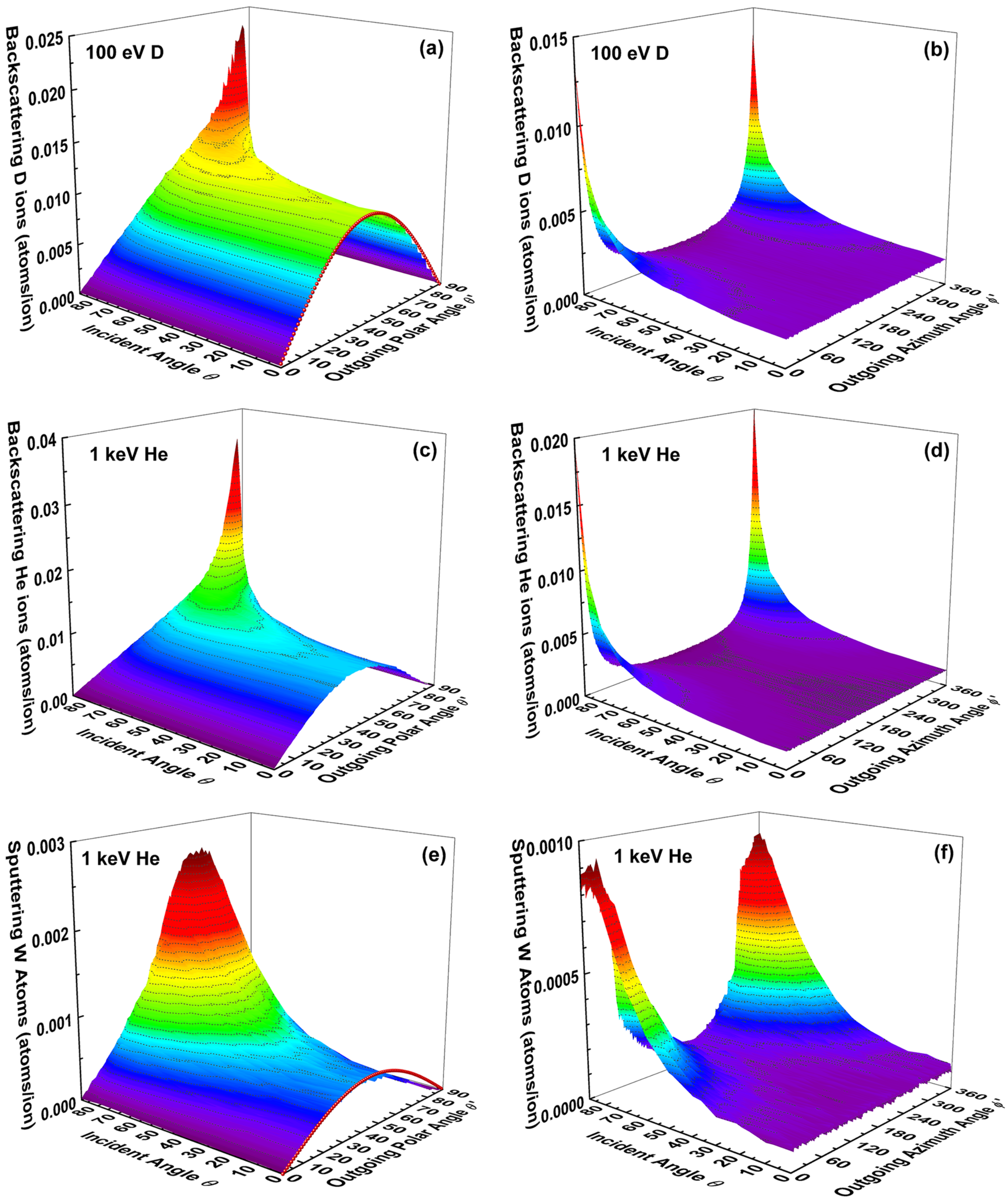

Figure 4. (a) Polar (θ') and (b) azimuthal (ϕ') angle distributions of backscattered D ions from smooth W surface under 100 eV D-ion irradiation with different incident angles (θ). (c) θ' and (d) ϕ' distributions of backscattered He-ions, and (e) θ' and (f) ϕ' distributions of sputtered W atoms from smooth W surface under 1 keV He-ion irradiation with different θ. The red lines in (a) and (e) show a sine fit to θ' at normal incidence (θ=0).

3.3 Rough W surface

First, 100 eV D-ion irradiation with finite surface roughness (3σ = 0-1000 nm, a = 50 nm) is simulated. The 3D spatial distribution of D-ion implantation I (i.e., the fraction of D-ion deposition in W to total D fluence) in the W surface is shown in figure 1(e). D-ions are mainly distributed in the near-surface region, several nm deep, and fluctuate along with the rough peaks and valleys. The depth-distribution of D in rough W at normal incidence and the relation of I with 3σ and θ are shown in figures 5(a) and (b), respectively. The D-ion depth distribution follows a Gaussian function, whose full width at half maximum (FWHM) increases with increasing 3σ and also nearly equals the FWHM of the surface roughness. This illustrates that the nano-geometric effect mainly influences ion implantation, and ion penetration depth is just another small contribution. As shown in figure 5(b), I increases with increasing 3σ and decreases with increasing θ. It is dominated by the interplay of backscattering enhancement with the effective incident angles α (related to 3σ and θ) and the shading effect by rough peaks for different roughness, as mentioned in the next section.

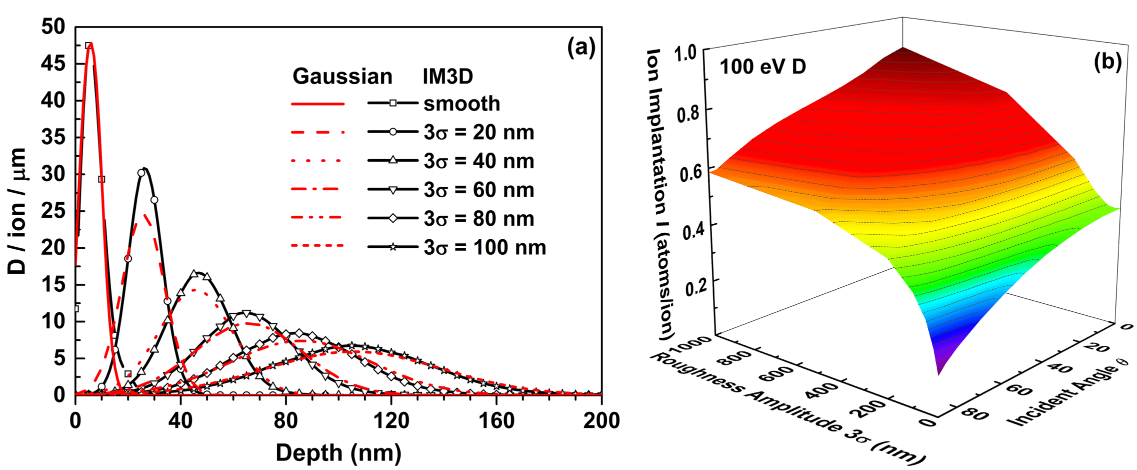

Figure 5. (a) D-ion depth distributions (black lines) for W rough surface with 3σ varying from 0-100 nm and a = 50 nm, under 100 eV random D-ion irradiation at normal incidence (θ=0). The depth-distribution of D is obtained by integrating D spatial distribution along the two orthogonal directions parallel to the surface. The red lines show the convolution of the Gaussian function with σ and D ion depth distribution for a smooth W surface. Here "0" depth is defined as Z equal to -3σ referring to the mean height of surface roughness. (b) D ion implantation I for W rough surface with 3σ varying from 0-1000 nm and a = 50 nm, under the irradiation of 100 eV random D-ion beam with different incident polar angles (θ).

Next, 1 keV He-ion sputtering of W is simulated using the same geometry, with the results given in figure 6. The same trend of increasing He-ion implantation with roughness and incident polar angles is shown in figure 6(a). Surface sputtering would occur when the energy of He ions used is high enough (> 107 eV). Accordingly, the variation of Y with 3σ and θ is shown in figure 6(b). The opposite trend is found compared to the relationship between I and 3σ and θ. Y for He-ions decreases with increasing σ, which is consistent with recent experiments (as shown in figure 7) [2, 12] except for a minor increase for 3σ < 50 nm at small θ. The minor increase of Y for 3σ < 50 nm at small θ is mainly due to the domination of sputtering enhancement compared to shading suppression. The reduction of Y with increasing σ comes mainly from direct line-of-sight deposition of a large fraction of low-energy sputtered atoms onto neighboring asperities [12]. In addition, there is a small decrease at θ > 85° for different σ, as shown in figure 3(b)), which is caused by increased ion backscattering at glancing θ.

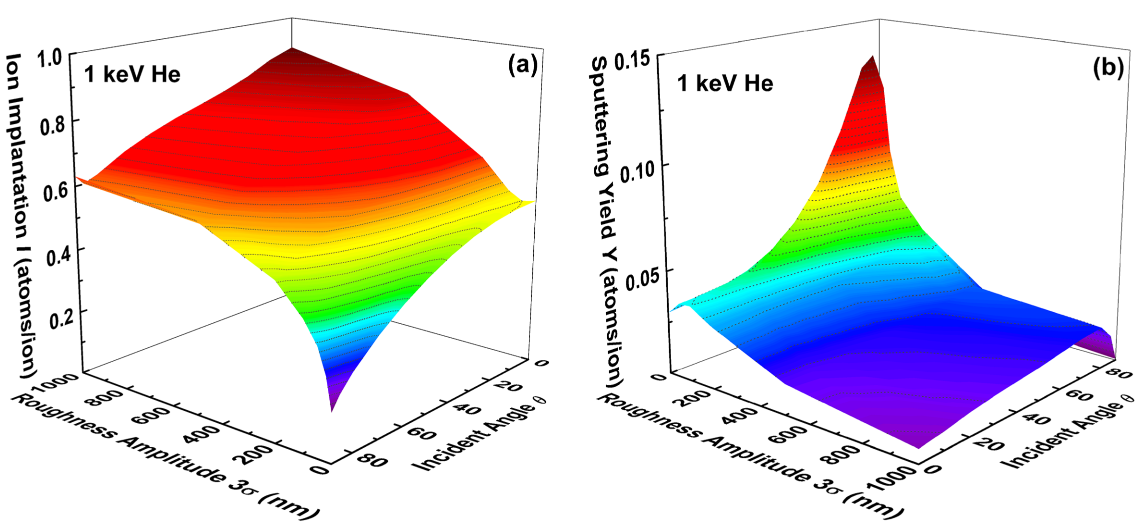

Figure 6. (a) He ion implantation I and (b) sputtering yields Y for W rough surface with 3σ varying from 0-1000 nm and a = 50 nm, under irradiation by 1 keV randomly-oriented He-ions with different incident polar angles (θ).

Thus, both low-roughness surfaces under ion irradiation with large incident polar angles and high-roughness surfaces under ion irradiation with small incident polar angles exhibit dramatically reduced ion implantation and sputtering of W, respectively. At 400-800 °C in ITER [8], implanted D/T/He atoms will diffuse quickly, some of which would desorb from the surface, while the other portion would be trapped by the enhanced interfacial area of the nanostructured surface [63]. It is a very complex dynamic process for retention of implanted ions in W in view of the simultaneous effects of ion implantation, diffusion and trapping at finite temperature and longer timescales. Moreover, the high surface area may further aggravate implanted-atom desorption. In fact, we have systematically investigated He [64, 65] and D [66, 67] retention behaviors in W with smooth surface by combining the binary collision and cluster dynamics models before. When the major contribution of diffusion and trapping to atom desorption is fixed, ion implantation however would be the only key factor left to affect retention of these species.

Finally, the reliability of IM3D's predictions is evaluated by comparing to existing experiments. As shown in figure 7, the sputtering yield of rough W (3σ from 0-2 μm) under 110 eV Ar-ion irradiation given by IM3D agrees well for small feature lengths L_t to that of fuzzy W by mass loss measurements, while larger features show less agreement. The sputtering yield of 0.046 atoms/ion was obtained for the smooth W surface, which agrees well with the TRIM.SP calculation [42] and measurements from ion beams [59] and plasma (0.05±0.002) [12]. The ratio $Y_{\mathrm{rough}}/Y_{\mathrm{smooth}}$ decreases with the increasing feature length L_t, which agrees with experiments [12] when taking a = 50 nm. In the experiment L_t denotes the fuzzy layer thickness measured from SEM cross-sections or estimated from the surface temperature and the plasma exposure time by a $t^{1/2}$ dependence, while in the simulation it is selected as the roughness amplitude 3σ which is on the same level of the measured layer thickness. Nishijima et al. pointed out that this trend is consistent with the change in the complementary fuzz porosity [12]. Because the fuzz porosity is a characteristic parameter of surface morphology and increases with L_t, it should thus have a similar trend with surface roughness amplitude. IM3D values are a little lower than that of experiment, which might come from the simplicity of its rough surface model and the underestimation of the rough peak interval a and the feature length L_t (~ 3σ). While it is difficult to determine an exact value of the experimental peak interval for different fuzzy structures, setting a to 50 nm should be physically reasonable, since the feature size of fuzzy structures is usually in the range of 10's of nm [37].

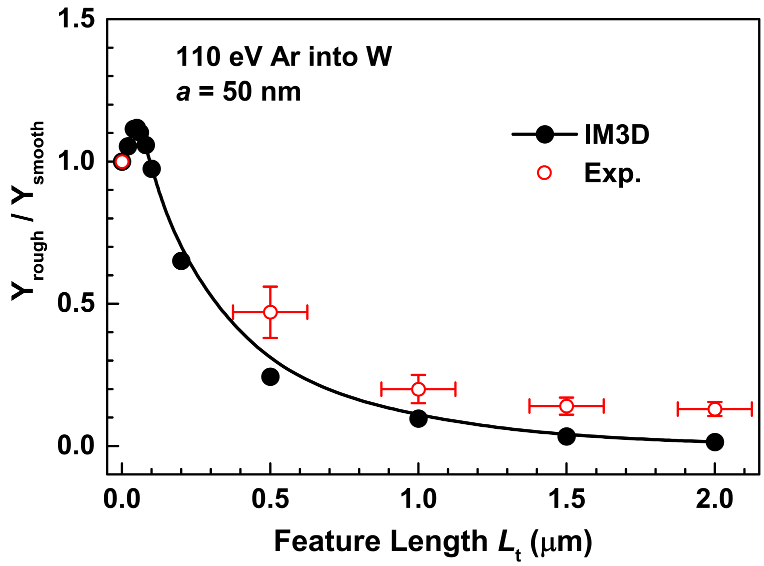

Figure 7. Comparison of IM3D-calculated sputtering yields $Y_{\text{rough}}/Y_{\text{smooth}}$ with experimental results [12], for 110 eV Ar-ion sputtering of W rough surfaces with a = 50 nm and feature length L_t ranging from 0-2 μm. A spline fitting line is also drawn to guide the reader's eye.

3.4 Connecting smooth-surface results with rough-surface results

In order to describe the analytical relationship of I vs. σ (the shading effect), a simple formula is proposed at normal incidence, as the black solid line in figures 8 and 9(a). As shown in figures 1(b) and (d), the slope angle α of a surface facet can be defined as $\alpha \equiv \arctan(\Delta Z/a)$, where ΔZ is the profile element height (the sum of the height of the peak and depth of the valley of a triangular element). The mean value of the slope angles, $\bar{\alpha}$, can be estimated by averaging with the Gaussian distribution for the rough surfaces with $3\sigma = 0$ - 1000 nm and $a = 50$ nm, as shown in SOM 2. As shown in figure 1(d), the effective incident angle of normal-incidence ($\theta = 0$) ions is approximately equal to α. Thus, to a zeroth-order approximation (only taking into account of the backscattering effect related to $\bar{\alpha}$ but not the shading effect due to rough peaks), the ion implantation is defined as (green dot line in figures 8 and 9(a)),

$$I_0(\bar{\alpha}) \equiv 1 - \eta\,(\bar{\alpha}), \tag{2}$$

where $\eta(\bar{\alpha})$ is the backscattering coefficient as a function of the mean effective incident angle (also equal to $\bar{\alpha}$ as defined in SOM 2), which was calculated by IM3D directly for an infinitely smooth surface (magenta, short dashed lines in figures 8 and 9(a)).

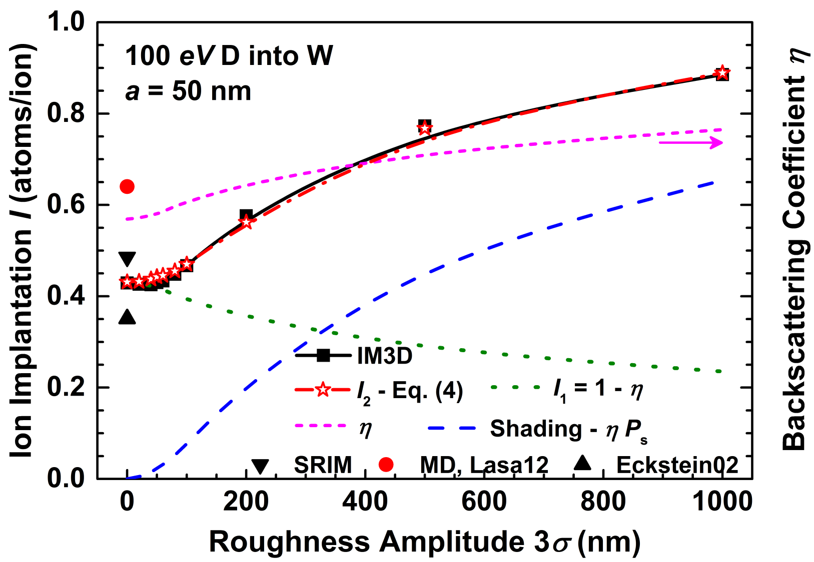

Figure 8. The D-ion implantation I calculated by IM3D and estimated by equation (4) using $3\sigma = 0$-1000 nm for W rough surface with $a = 50$ nm. 100 eV D-ion beam with random normal-incidence is applied here. The SRIM (calculated by SRIM-2013 [32] with default settings), TRIM.SP [42] and MD [48] values of D-ion implantation for a smooth surface are also given for comparison.

In fact, a fraction of backscattered ions would be shaded by surface asperities. Only backscattered ions exiting within a critical polar angle range $\theta' < (90^{\circ} - \bar{\alpha}) + \arctan\left[\left(2a - Z \cdot \tan(90^{\circ} - \bar{\alpha})\right)/Z\right]$ could be shaded as discussed in SOM 3. The emission probability or the complementary shading probability (P_s) are thus estimated by numerically integrating the exact angular distribution of outgoing ions within the emission solid angle, and from zero to the mean profile element height $\overline{\Delta Z}$ of rough peaks, as shown in figures 8 and 9(a) (blue dashed line) and discussed in SOM 3. The angular distribution of backscattered ions/sputtered atoms is anisotropic related to the incident energies and directions of ions as shown in refs. [12, 44, 45] and in SOM 3, which has been already included in the estimation of P_s automatically. Therefore, if we suppose that all the shaded ions are deposited in asperities as a first-order approximation, the ion implantation can be described by,

$$I_1 = 1 - \eta(\bar{\alpha}) + \eta(\bar{\alpha}) \cdot P_s. \tag{3}$$

If we consider that there is still some probability for the shaded ions to escape from asperities, a more accurate estimation of the ion implantation in roughness surface can be given by a second-order approximation,

$$I_2 = 1 - \eta(\bar{\alpha}) + R_2^0 \cdot \eta(\bar{\alpha}) \cdot P_s. \tag{4}$$

Here, the secondary implantation $I_2^0 = 1 - \eta(\bar{\alpha}) + I_1 \cdot \eta(\bar{\alpha}) \cdot P_s$ (I_1 is used as an initial guess), as I_2^0 should be smaller than I_1 due to the lower energies and shading probability of secondary ions. In fact, this approximation is more reasonable for large σ, as discussed in SOM 4.

As shown in figures 8 and 9(a), a good agreement has been reached between the IM3D results (black solid line) and the estimations by equation (4) (red line), which illustrates that the relationship proposed here is quite robust. Under the critical roughness amplitude of $3\sigma = 50$ nm, the backscattering effect $\eta(\bar{\alpha})$ dominates the primary ion implantation in W. The shading effect appears after $3\sigma > 50$ nm, and becomes more important to ion implantation in W with increasing 3σ. The interplay between these two effects changes the ion implantation in rough W. The small deviation between the calculated and analytical results mainly comes from the estimation of R_2 when employing I_2^0 for lower-energy secondary backscattered ions, as discussed in SOM 4.

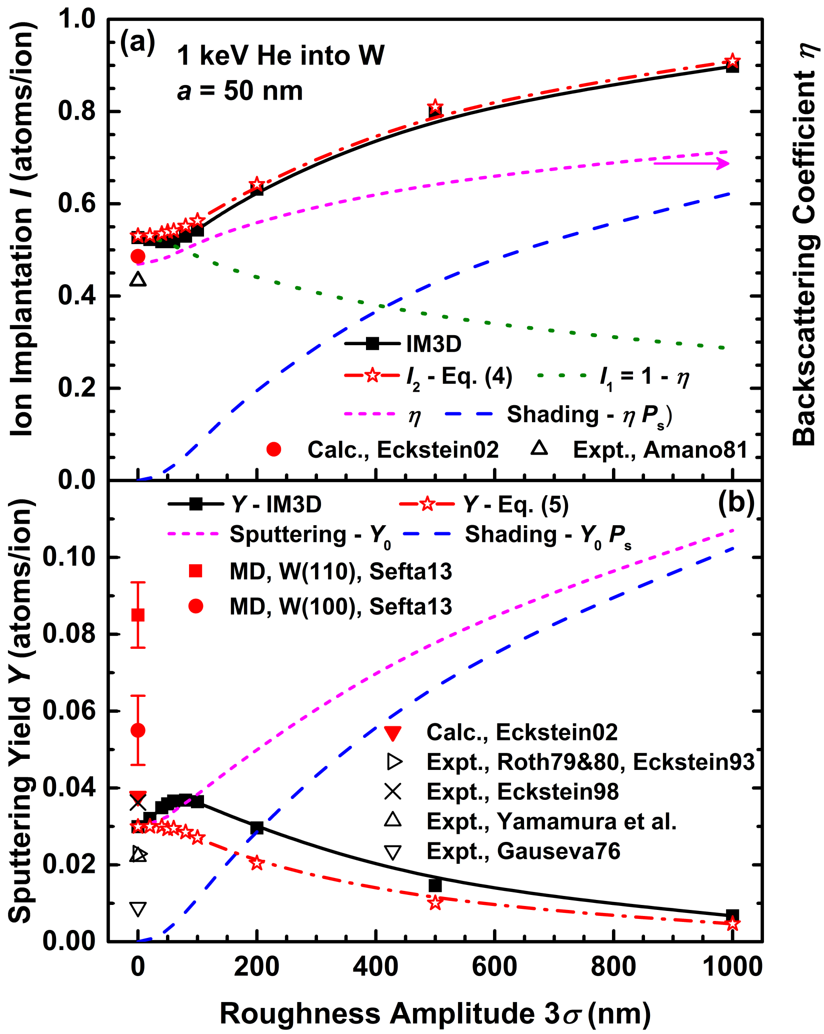

Figure 9. (a) The He-ion implantation I calculated by IM3D and estimated by equation (4), as well as (b) the sputtering yield Y calculated by IM3D and estimated by equation (5), along with 3σ from 0-1000 nm for rough W with a = 50 nm. 1 keV He ion beam with random normal-incidence is applied here. The TRIM.SP [42] and experimental values [49] of He-ion implantation I_0 as well as the TRIM.SP [42], MD [46, 50] and experimental values [51-58] of He sputtering yields Y_0 for smooth surface are also given for comparison.

Similarly, the relationship of Y vs. σ can also be described by a simple analytical expression, by taking into account the shading (P_s) of primary sputtered W atoms by surface asperities,

$$Y = A(\bar{\alpha}) \cdot Y_0(\bar{\alpha}) \cdot (1 - P_s), \tag{5}$$

where $Y_0(\bar{\alpha})$ is the $\bar{\alpha}$-dependent sputtering yield of the smooth surface as shown in figure 3(b). $A(\bar{\alpha})$ is an $\bar{\alpha}$-dependent coefficient relating the secondary sputtering to reflected He ions or sputtered W atoms, which would increase with increasing $Y_0(\bar{\alpha})$ and reach a saturation value quickly. $A(\bar{\alpha})$ is much complicated for random rough surfaces, but saturates quickly due to the shading rate approaching unity at high σ, as discussed in SOM 4. For simplicity, we neglect the secondary sputtering effect here and set $A(\bar{\alpha})=1$, as the emitted atoms could induce less serious secondary surface sputtering when their mean energy is close to/under the threshold energy that can cause W sputtering. In figure 9(b), a consistent trend between IM3D and equation (5) is obtained except for an underestimation of values due to the exclusion of secondary sputtering in the analytical expression. In fact, the secondary sputtering effect will induce about 45% extra sputtered atoms for rough W under 1 keV He-ion irradiation, as shown in SOM 4.

4. Summary and discussions

Ion implantation can be enhanced by a factor of two with rough surfaces compared to smooth surface depending on roughness amplitude, while the sputtering yield of the rough surface is around one order of magnitude lower than that of the smooth surface due to recapture by adjacent peaks. This enhancement of ion absorption (the enhancement of ion implantation and the reduction of ion sputtering) due to surface roughness, called the ion radiation albedo effect, is mainly determined by the nano-geometric shading process and less dependent on the type and energy of incident ions. In addition, according to the proposed simple analytical formulas (Eqs. (4) and (5)), one can more clearly understand the contribution factors to ion implantation and sputtering for different rough surfaces or even any other types of nano-arrays. Ion implantation and sputtering yields of a typical rough surface can also be estimated by providing only the incident and emission angle-dependent ion backscattering coefficient and sputtering yield of the smooth surface, respectively, instead of constructing a complex surface model. Furthermore, for both smooth and rough surfaces, increasing the angle of incidence further increases ion backscattering and sputtering (except for a small decrease in sputtering at glancing incidence) due to the backscattering enhancement, which also influences the ion radiation albedo effect.

In general, in fusion engineering the radiation albedo effect is deleterious by enhancing ion implantation but beneficial by reducing ion sputtering for PFMs like W. Moreover, this effect could be beneficial in other contexts, for example ion beam processing of surfaces to induce high surface area and light absorption, such as photo-electrochemical water splitting, solar energy conversion, and pyroelectric detectors [2, 68-70].

Acknowledgements

This work was supported by the National Natural Science Foundation of China under Grant Nos. 11275229, 11475215 & NSAF U1230202, the key project of National Science Foundation of China under Grant No. 11534012, the Special Funds for Major State Basic Research Project of China (973) under Grant No. 2012CB933702, the Youth Innovation Promotion Association of CAS under Grant No. 2016386, and Director Grants of CASHIPS. Part of the calculations were performed at the Center for Computational Science of CASHIPS, the ScGrid of Supercomputing Center, and the Computer Network Information Center of the Chinese Academy of Sciences. JL and YY acknowledge support by NSF DMR-1410636 and DMR-1120901. MPS acknowledges support by the U.S. Nuclear Regulatory Commission (NRC), under grant number NRC-HQ-84-15-G-0045. Computational time on the Extreme Science and Engineering Discovery Environment (XSEDE) under the grant number TG-DMR130038 is gratefully acknowledged. ZD acknowledge support by National Natural Science Foundation of China (Nos 11274288 & 11574289), Ministry of Education of China (No. 20123402110034) and "111" project (No. B07033).

References

[1] Krasheninnikov A.V. and Nordlund K. 2010 Ion and electron irradiation-induced effects in nanostructured materials *J. Appl. Phys.* **107** 071301

[2] Tanyeli I., Marot L., Mathys D., van de Sanden M.C. and De Temmerman G. 2015 Surface modifications induced by high fluxes of low energy helium ions *Sci. Rep.* **5** 9779

[3] Krauz V.I., Martynenko Y.V., Svechnikov N.Y., Smirnov V.P., Stankevich V.G. and Khimchenko L.N. 2011 Nanostructures in controlled thermonuclear fusion devices *Physics-Uspekhi* **53** 1015-1038

[4] Dhara S. 2007 Formation, dynamics, and characterization of nanostructures by ion beam irradiation *Crit. Rev. Solid State Mater. Sci.* **32** 1-50

[5] Federici G., Skinner C.H., Brooks J.N., Coad J.P., Grisolia C., Haasz A.A., Hassanein A., Philipps V., Pitcher C.S, Roth J., Wampler W.R. and Whyte D.G. 2001 Plasma-material interactions in current tokamaks and their implications for next step fusion reactors *Nucl. Fusion* **41** 1967-2137

[6] Roth J., Tsitrone E., Loarte A., Loarer Th., Counsell G., Neu R., Philipps V., Brezinsek S., Lehnen M., Coad P., Grisolia Ch., Schmid K., Krieger K., Kallenbach A., Lipschultz B., Doerner R., Causey R., Alimov V., Shu W., Ogorodnikova O., Kirschner A., Federici G. and Kukushkin A. EFDA PWI Task Force, ITER PWI Team, Fusion for Energy, ITPA SOL/DIV. 2009 Recent analysis of key plasma wall interactions issues for ITER *J. Nucl. Mater.* **390-391** 1-9

[7] Nordlund K., Björkas C., Ahlgren T., Lasa A. and Sand A.E. 2014 Multiscale modelling of plasma–wall interactions in fusion reactor conditions *J. Phys. D: Appl. Phys.* **47** 224018

[8] Wirth B.D., Hammond K.D., Krasheninnikov S.I. and Maroudas D. 2015 Challenges and opportunities of modeling plasma–surface interactions in tungsten using high-performance computing *J. Nucl. Mater.* **463** 30-38

[9] Kajita S., Sakaguchi W., Ohno N., Yoshida N. and Saeki T. 2009 Formation process of tungsten nanostructure by the exposure to helium plasma under fusion relevant plasma conditions *Nucl. Fusion* **49** 095005

[10] Sandoval L., Perez D., Uberuaga B.P. and Voter A.F. 2015 Competing kinetics and He bubble morphology in W *Phys. Rev. Lett.* **114** 105502

[11] Lasa A., Tähtinen S. K. and Nordlund K. 2014 Loop punching and bubble rupture causing surface roughening—A model for W fuzz growth *EPL (Europhys. Lett.)* **105** 25002

[12] Nishijima D., Baldwin M.J., Doerner R.P. and Yu J.H. 2011 Sputtering properties of tungsten 'fuzzy' surfaces *J. Nucl. Mater.* **415** S96-S99

[13] Frost F., Ziberi B., Schindler A. and Rauschenbach B. 2008 Surface engineering with ion beams: from self-organized nanostructures to ultra-smooth surfaces *Appl. Phys. A* **91** 551-559

[14] Kajita S., Saeki T., Yoshida N., Ohno N. and Iwamae A. 2010 Nanostructured Black Metal: Novel Fabrication Method by Use of Self-Growing Helium Bubbles *Appl. Phys. Express* **3** 085204

[15] El-Atwani O., Gonderman S., Efe M., Gregory D.T., Morgan T., Bystrov K., Klenosky D., Qiu T. and Allain J.P. 2014 Ultrafine tungsten as a plasma-facing component in fusion devices: effect of high flux, high fluence low energy helium irradiation *Nucl. Fusion* **54** 083013

[16] 't Hoen M.H.J., Balden M., Manhard A., Mayer M., Elgeti S., Kleyn A.W. and Zeijlmans van Emmichoven P.A. 2014 Surface morphology and deuterium retention of tungsten after low- and high-flux deuterium plasma exposure *Nucl. Fusion* **54** 083014

[17] Wei Q., Eddy M., Li K.D. and Wang L. 2009 Influence of surface morphology on sputtering yields *J. Phys. D: Appl. Phys.* **42** 165304

[18] Doerner R.P., Björkas C., Nishijima D. and Schwarz-Selinger T. 2013 Erosion of beryllium under high-flux

plasma impact *J. Nucl. Mater.* **438** S272–S275

[19] Doerner R.P., Nishijima D. and Schwarz-Selinger T. 2014 Impact of surface morphology on sputtering during high-fluence plasma exposure *Phys. Scr.* **T159** 014040

[20] Doerner R.P., Nishijima D. and Schwarz-Selinger T. 2012 Measuring the difference between gross and net erosion *Nucl. Fusion* **52** 103003

[21] Doerner R.P., Jepu I., Nishijima D., Safi E., Bukonte L., Lasa A., Nordlund K. and Schwarz-Selinger T. 2015 The relationship between gross and net erosion of beryllium at elevated temperature *J. Nucl. Mater.* **463** 777–780

[22] Ogorodnikova O.V., Roth J. and Mayer M. 2008 Ion-driven deuterium retention in tungsten *J. Appl. Phys.* **103** 034902

[23] Alimov V.K. and Roth J. 2007 Hydrogen isotope retention in plasma-facing materials: review of recent experimental results *Phys. Scripta* **T128** 6-13

[24] Bizyukov I., Krieger K., Lee H., Schmid K., Haasz A.A. and Davis J.W. 2012 An overview of sputtering-related processes occurring at mixed surfaces formed by simultaneous C^+ and D^+ irradiation of W *J. Nucl. Mater.* **427** 401-410

[25] Gonzalez-Arrabal R., Panizo-Laiz M., Gordillo N., Tejado E., Munnik F., Rivera A. and Perlado J.M. 2014 Hydrogen accumulation in nanostructured as compared to the coarse-grained tungsten *J. Nucl. Mater.* **453** 287-295

[26] Sigmund P. 1969 Theory of sputtering. I. Sputtering yield of amorphous and polycrystalline targets *Phys. Rev.* **184** 383-416

[27] Kustner M., Eckstein W., Hechtl E. and Roth J. 1999 Angular dependence of the sputtering yield of rough beryllium surfaces *J. Nucl. Mater.* **265** 22-27

[28] Molodtsov S.L., Gurbich A.F. and Jeynes C. 2008 Accurate ion beam analysis in the presence of surface roughness *J. Phys. D: Appl. Phys.* **41** 205303

[29] Ruzic D.N. 1990 The effects of surface roughness characterized by fractal geometry on sputtering *Nucl. Inst. Meth. Phys. Res. B* **47** 118-125

[30] Kenmotsu T., Yamamura Y., Muramoto T. and Hirotani N. 2005 Simulation studies on sputtering in rough surface *Nucl. Inst. Meth. Phys. Res. B* **228** 369-372

[31] Hu A. and Hassanein A. 2012 How surface roughness affects the angular dependence of the sputtering yield *Nucl. Inst. Meth. Phys. Res. B* **281** 15-20

[32] Ziegler J.F., Ziegler M.D. and Biersack J.P. 2010 SRIM – The stopping and range of ions in matter. *Nucl. Inst. Meth. Phys. Res. B* **268** 1818-1823; SRIM website, http://www.srim.org

[33] Li Y.G., Yang Y., Short M.P., Ding Z.J., Zeng Z. and Li J. 2015 IM3D: A parallel Monte Carlo code for efficient simulations of primary radiation displacements and damage in 3D geometry *Sci. Rep.* **5** 18130 (Website,

http://theory.issp.ac.cn/IM3D, http://Li.mit.edu/im3d and https://github.com/shortlab/IM3D).

[34] Li Y.G., Mao S.F., Li H.M., Xiao S.M. and Ding Z.J. 2008 Monte Carlo simulation study of scanning electron microscopy images of rough surfaces *J. Appl. Phys.* **104** 064901

[35] Kinchin G.H. and Pease R.S. 1955 The displacement of atoms in solids by radiation *Rep. Prog. Phys.* **18** 1–51

[36] Norgett M.J., Robinson M.T. and Torrens I.M. 1975 A proposed method of calculating displacement dose rates *Nucl. Eng. Des.* **33** 50–54

[37] Fiflis P., Curreli D. and Ruzic D. N. 2015 Direct time-resolved observation of tungsten nanostructured growth due to helium plasma exposure *Nucl. Fusion* **55** 033020

[38] Li H.M. and Ding Z.J. 2005 Monte Carlo simulation of secondary electron and backscattered electron images in scanning electron microscopy for specimen with complex geometric structure *Scanning* **27** 254–267

[39] Li Y.G., Ding Z.J. and Zhang Z.M. 2009 Monte Carlo simulation study of scanning Auger electron images *J. Appl. Phys.* **106** 024316

[40] Zhang P., Wang H.Y., Li Y.G., Mao S.F. and Ding Z.J. 2012 Monte Carlo simulation of secondary electron images for real sample structures in scanning electron microscopy *Scanning* **34** 145-150

[41] Da B., Mao S.F., Zhang G.H., Wang X.P. and Ding Z.J. 2012 Monte Carlo modeling of surface excitation in reflection electron energy loss spectroscopy spectrum for rough surfaces *J. Appl. Phys.* **112** 034310

[42] Eckstein W. 2002 *Calculated Sputtering, Reflection and Range Values (IPP 9/132).* Garching, Max-Planck-Institute für Plasmaphysik. Online link: http://hdl.handle.net/11858/00-001M-0000-0027-4522-5

[43] Eckstein W. 2009 *Reflection (backscattering) (IPP 17/12)*. Garching, Max-Planck-Institute für Plasmaphysik. Online link: http://hdl.handle.net/11858/00-001M-0000-0026-F340-E

[44] Borovikov V., Voter A.F. and Tang X.Z. 2014 Reflection and implantation of low energy helium with tungsten surfaces *J. Nucl. Mater.* **447** 254-270

[45] Hofsäss H., Zhang K. and Mutzke A. 2014 Simulation of ion beam sputtering with SDTrimSP, TRIDYN and SRIM *Appl. Surf. Sci.* **310** 134-141

[46] Ferroni F., Hammond K.D. and Wirth B.D. 2015 Sputtering yields of pure and helium-implanted tungsten under fusion-relevant conditions calculated using molecular dynamics *J. Nucl. Mater.* **458** 419-424

[47] Hofsäss H., Bobes O. and Zhang K. 2013 Is sputtering relevant for ion-induced self-organized pattern formation? *AIP Conf. Proc.* **1525** 386-391

[48] Lasa A., Björkas C., Vörtler K. and Nordlund K. 2012 MD simulations of low energy deuterium irradiation on W, WC and surfaces *J. Nucl. Mater.* **429** 284-292

[49] Amano J. and Seidman D.N. 1981 Experimental determination of the particle reflection coefficients of low-energy (100-1500 eV) ^{3}He and ^{4}He atoms from the (110) plane of tungsten *J. Appl. Phys.* **52** 6934

[50] Sefta F., Juslin N., Hammond K.D. and Wirth B.D. 2013 Molecular dynamics simulations on the effect of sub-surface helium bubbles on the sputtering yield of tungsten *J. Nucl. Mater.* **438** S493-S496

[51] Roth J., Bohdansky J. and Ottenberger W. 1979 *Data on low energy light ion sputtering (IPP 9/26)*. Garching, Max-Planck-Institute für Plasmaphysik. Online link: http://hdl.handle.net/11858/00-001M-0000-0027-6AE6-7

[52] Roth J., Bohdansky J. and Martinelli A.P. 1980 Low energy light ion sputtering of materials and carbides *Radiat. Eff.* **48** 213-219

[53] Eckstein W., Garcia-Rosales C., Roth J. and Ottenberger W. 1993 *Sputtering data (IPP 9/82)*. Garching, Max-Planck-Institute für Plasmaphysik. Online link: http://hdl.handle.net/11858/00-001M-0000-0027-6324-6

[54] Eckstein W. 1998 *Sputtering, reflection and range values for plasma edge codes (IPP 9/117)*. Garching, Max-Planck-Institute für Plasmaphysik. Online link: http://hdl.handle.net/11858/00-001M-0000-0027-6091-4

[55] Yamamura Y. and Tawara H. 1995 *Energy dependence of ion-induced sputtering yields from monoatomic solids at normal incidence*, Report NIFS-DATA-23

[56] Yamamura Y., Sakaoka K. and Tawara H. 1995 *Computer simulation and data compilation of sputtering yields by hydrogen isotopes ($^1H^+$, $^2D^+$, $^3T^+$) and helium ($^4He^+$) ion impact from monoatomic solids at normal incidence*, Report NIFS-DATA-31

[57] Yamamura Y. and Tawara H. 1996 Energy dependence of ion-induced sputtering yields from monoatomic solids at normal incidence *Atom. Data & Nucl. Data Tab.* **62** 149-253

[58] Gauseva M.I. and Martynenko Y.V. 1976 *Fiz. Plaz.* **2** 593

[59] Eckstein W. 2007 *Sputtering yields. In: Sputtering by Particle Bombardment* eds Behrisch R. and Eckstein W. (Springer-Verlag)

[60] Stoller R.E., Toloczko M.B., Was G.S., Certain A.G., Dwaraknath S. and Garner F.A. 2013 On the use of SRIM for computing radiation damage exposure *Nucl. Inst. Meth. Phys. Res. B* **310** 75–80

[61] Sugiyama K., Schmid K., Jacob W. 2016 Sputtering of iron, chromium and tungsten by energetic deuterium ion bombardment *Nucl. Mater. Ene.* **8** 1–7

[62] Eckstein W., Verbeek H. and Biersack J.P. 1980 Computer simulation of the backscattering and implantation of hydrogen and helium *J. Appl. Phys.* **51** 1194-1200

[63] Ackland G. 2010 Controlling radiation damage *Science* **327** 1587-1588

[64] Li Y.G., Zhou W.H., Ning R.H., Huang L.F., Zeng Z. and Ju X. 2012 A cluster dynamics model for accumulation of helium in tungsten under helium ions and neutron irradiation *Commun. Comput. Phys.* **11** 1547-1568

[65] Li Y.G., Zhou W.H., Huang L.F., Zeng Z. and Ju X. 2012 Cluster dynamics modeling of accumulation and diffusion of helium in neutron irradiated tungsten *J. Nucl. Mater.* **431** 26–32

[66] Ning R.H. Li Y.G., Zhou W.H., Zeng Z. and Xin J. 2012 An improved cluster dynamics model for hydrogen retention in tungsten *Inter. J. Modern Phys. C* **23** 1250042

[67] Ning R.H., Li Y.G., Zhou W.H., Zeng Z. and Ju X. 2012 Modeling D retention in W under D ions and neutrons irradiation *J. Nucl. Mater.* **430** 20–26

[68] de Respinis M., De Temmerman G., Tanyeli I., van de Sanden M.C.M., Doerner R.P., Baldwin M.J. and van de Krol R. 2013 Efficient plasma route to nanostructure materials: case study on the use of m-WO3 for solar water splitting *ACS Appl. Mater. Interfaces* **5** 7621-7625

[69] Brown R.J.C., Brewer P.J. and Milton M.J.T. 2002 The physical and chemical properties of electroless nickel-phosphorus alloys and low reflectance nickel-phosphorus black surfaces *J. Mater. Chem.* **12(9)** 2749-2754

[70] Yang Z.P., Ci L.J., Bur J.A., Lin S.Y. and Ajayan P.M. 2008 Experimental observation of an extremely dark material made by a low-density nanotube array *Nano. Lett.* **8** 446-451